



## Retrieving middle-infrared reflectance for burned area mapping in tropical environments using MODIS

Renata Libonati<sup>a,c,\*</sup>, Carlos C. DaCamara<sup>a</sup>, José Miguel C. Pereira<sup>b</sup>, Leonardo F. Peres<sup>c</sup>

<sup>a</sup> University of Lisbon, IDL/CGUL, Lisbon, Portugal

<sup>b</sup> School of Agronomy, Technical University of Lisbon, Lisbon, Portugal

<sup>c</sup> Center for Weather Forecast and Climate Studies, Brazilian National Institute for Space Research, Cachoeira Paulista, Brazil

### ARTICLE INFO

#### Article history:

Received 10 July 2009

Received in revised form 23 November 2009

Accepted 28 November 2009

#### Keywords:

Reflectance retrieval

Middle-infrared

Tropics

Burned area

Remote sensing

### ABSTRACT

The ephemeral character of the radiative signal together with the presence of aerosols imposes severe limitations on the use of classical approaches, e.g. based on red and near-infrared, to discriminate between burned and unburned surfaces in tropical environments. Surface reflectance in the middle-infrared (MIR) has been used to circumvent these difficulties because the signal is virtually unaffected by the presence of aerosols associated to biomass burning. Retrieval of the MIR reflected component from the total signal is, however, a difficult problem because of the presence of a diversity of radiance sources, namely the surface reflected solar irradiance and the surface emitted radiance that may reach comparable magnitude during daytime. The method proposed by Kaufman and Remer (1994) to retrieve surface MIR reflectance presents the advantage of not requiring auxiliary datasets (e.g. atmospheric profiles) nor major computational means (e.g. for solving radiative transfer models). Nevertheless, the method was specifically designed to retrieve MIR reflectance over dense dark forests in the middle latitudes and, as shown in the present study, severe problems may arise when applying it beyond the range of validity, namely for burned area mapping in tropical environments. The present study consists of an assessment of the performance of the method for a wide range of atmospheric, geometric and surface conditions and of the usefulness of extracted surface reflectances for burned area discrimination. Results show that, in the case of tropical environments, there is a significant decrease in performance of the method for high values of land surface temperature, especially when associated with low sun elevation angles. Burned area discrimination is virtually impaired in such conditions, which are often present when using data from instruments on-board polar orbiters, namely MODIS in Aqua and Terra, to map burned surfaces over the Amazon forest and “cerrado” savanna regions.

© 2009 Elsevier Inc. All rights reserved.

### 1. Introduction

Over the last decade continuous monitoring of vegetation fires from space has greatly contributed to an increased recognition of the major role played by biomass burning in climate change. In fact, biomass burning is a global source of greenhouse gases (e.g. CO<sub>2</sub> and CH<sub>4</sub>) as well as of CO, NO<sub>2</sub>, NO<sub>x</sub>, CH<sub>3</sub>Br and hydrocarbons involved in the formation of acid rain, in the photochemical production of tropospheric ozone and in the destruction of stratospheric ozone (e.g. Crutzen & Andreae, 1990; Penner et al., 1992). At the regional level, biomass burning may induce changes in atmospheric stability and associated vertical motions, leading to alterations of the hydrologic cycle with significant impacts on regional climate (e.g. Rosenfeld, 1999; Menon et al., 2002; Koren et al., 2004). Teleconnection processes may also take place, inducing changes e.g. of rainfall and surface temperature patterns across distant parts of the world (Chase

et al., 2000; Zhao et al., 2001; Pielke et al., 2002). In particular, the study by Evangelista et al. (2007) suggests that almost half of the aerosol black carbon in the South-West Atlantic may derive from South American biomass burning. In addition, vegetation fires are one of the most important causes of land use/cover dynamics (Lambin & Geist, 2006), destroying and altering vegetation structure and depositing charcoal and ash on the surface. Such changes may, in turn, lead to modifications in the physical properties of the surface such as the ratio of latent to sensible heat flux, the transfer of momentum from the atmosphere and the flux of moisture through evaporation and transpiration (Sellers et al., 1996; Jin & Roy, 2005).

Accordingly, a considerable number of environmental studies and Earth resources management activities require an accurate identification of burned areas. However, due to the very broad spatial extent and the limited accessibility of some of the largest areas affected by fire, instruments on-board satellites are currently the only available operational systems capable to collect cost-effective burned area information at adequate spatial and temporal resolutions (Pereira, 1999). This is especially true in the tropics, where most burning take place every year (Le Page et al., 2007). For instance, the Amazon

\* Corresponding author. University of Lisbon, IDL/CGUL, Lisbon, Portugal.  
E-mail address: [rlsantos@fc.ul.pt](mailto:rlsantos@fc.ul.pt) (R. Libonati).

region together with the adjacent savanna (“cerrado”) presents one of the highest numbers of occurrences of fire events (Prins et al., 1998).

Over the Amazon region the traditional use of red (R) and near-infrared (NIR) channels for detecting burned areas is severely impaired by the presence of heavy smoke layers due to biomass burning, since both channels are very sensitive to aerosol scattering and absorption in the atmosphere (Fraser & Kaufman, 1985; Holben et al., 1992; França & Setzer, 1998). A possible way to mitigate the aerosol effects associated to biomass burning on Earth observation from space is by using the middle-infrared (MIR) region (between 3.5 and 4.1  $\mu\text{m}$ ), since this part of the spectrum is also sensitive to vegetation changes but is virtually unaffected by the presence of most aerosols. However, Boyd and Duane (2001) pointed out that the use of MIR for studying the Earth’s surface properties at and beyond the regional scale may be unreliable. They further suggest that, in the case of tropical forests at regional to global scales, it may be preferable to only rely on the reflected component of MIR, since the emitted component of the signal may be subject to additional confounding variables, rather than representing intrinsic surface properties (Kaufman & Remer, 1994). Though related to tropical forest canopy properties, emitted radiation may also be influenced by a wide range of factors that include: i) localized atmospheric conditions such as wind speed and water vapor conductance (Price, 1989), ii) site-specific factors such as topography (Florinsky et al., 1994) and iii) soil moisture conditions (Luvall & Holbo, 1991; Nemani et al., 1993).

A large number of studies have shown that use of MIR reflectance is promising for a variety of applications such as discriminating among different vegetation types (Holben & Shimabukuro, 1993; Shimabukuro et al., 1994; Goita & Royer, 1997); estimating the total biomass and leaf biomass of several forest ecosystems (Boyd, 1999; Boyd et al., 2000); and monitoring the intra- and inter-annual changes in vegetation induced by climatic factors (Boyd & Duane, 2001). In particular, the work of Pereira (1999) showed that spectral vegetation indices using the R and NIR allow for improved burned/unburned area discrimination when the R channel is replaced by the reflected component of the MIR channel. Although use of the reflected component of MIR appears very attractive, its retrieval poses several challenging problems due to the presence, in a single measurement, of a diversity of radiance sources, namely linked to the thermal emission and the solar reflection from the atmosphere and by the surface. For instance, during daytime, the MIR surface reflected solar irradiance and the surface emitted radiance in MIR have comparable magnitude (Li & Becker, 1993).

Several methods have been proposed to solve the difficult problem of retrieving MIR reflectance from the total signal measured by a remote sensing instrument (e.g. Schutt & Holben, 1991; Li & Becker, 1993; Goita & Royer, 1997; Nerry et al., 1998; Roger & Vermote, 1998; Petitcolin & Vermote, 2002). All mentioned methods allow for the retrieval of MIR reflectance with acceptable accuracy, but most are time consuming, and normally require auxiliary datasets (e.g. atmospheric profiles) as well as intensive computational means (e.g. for solving radiative transfer computations). Kaufman and Remer (1994) proposed a different approach for retrieving MIR reflectance without direct knowledge of the atmospheric state and with no need for a radiative transfer model. Their method was originally designed to identify dense, dark vegetation areas in mid-latitude environments and the authors specifically stressed the need for further studies under different atmospheric conditions, as well as for other types of surface. The method has been applied in a number of studies involving both temperate and tropical conditions (e.g. Holben & Shimabukuro, 1993; Boyd, 1999; Boyd & Duane, 2001; Cihlar et al., 2004).

In particular, the approach proposed by Kaufman and Remer (1994), hereafter referred to as KR94, has been applied for burned area discrimination, since the MIR spectral domain may contribute to solving certain ambiguities between burned and unburned surfaces. These occur, for example, when using information from other parts of

the electromagnetic spectrum, namely the short-wave infrared (SWIR), especially between 2.0 and 2.5  $\mu\text{m}$  (França & Setzer, 2001). As shown in Fig. (1), the increase in reflectance over burned surfaces is higher in MIR than in SWIR, allowing a better discrimination between both surfaces. For instance, Pereira (1999) showed the added value of the method developed by KR94 in a pioneering study aiming to assess the ability of various vegetation indices to discriminate between burned and unburned surfaces in Portugal. The same methodology was used by Barbosa et al. (1999) and by Roy et al. (1999) to extract the reflective part of Advanced Very High Resolution Radiometer (AVHRR) channel 3, for input to algorithms aiming to map burned areas in Africa.

Results from the above-mentioned studies are certainly relevant, useful and promising; nevertheless, to the best of our knowledge, no assessment has discussed in depth the accuracy of the methodology proposed by KR94 when used to discriminate burned areas in tropical environments. Approximate solutions, like that proposed by KR94, are fast and easy to implement, but may be insufficiently accurate under specific surface and atmospheric conditions. The aim of the present study is to assess the quality and limitations of the retrieved MIR reflectance by means of KR94’s method when applied to discriminate burned areas in tropical environments.

Accordingly, the main objectives of the analysis are twofold:

1. To perform a quality assessment of MIR reflectance when retrieved using the algorithm proposed by KR94, for a wide range of atmospheric, geometric and surface conditions;
2. To assess the adequacy and limitations of the above-mentioned algorithm when applied to burned area discrimination, in particular in the Amazon and “cerrado” regions. Special attention will be devoted to the Moderate Resolution Imaging Spectrometer (MODIS) sensor, because of its widespread use in operational applications at the Brazilian National Institute for Space Research (INPE).

## 2. Rationale

One of the major difficulties encountered in the tropics when discriminating burned areas relates to the ephemeral character of

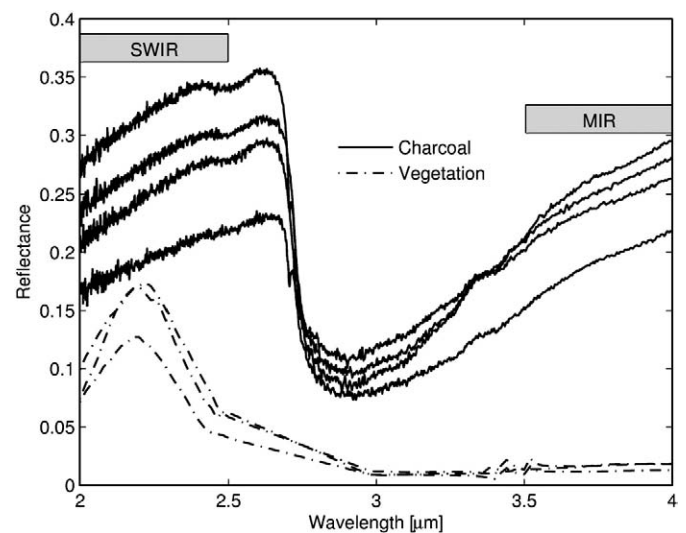


Fig. 1. Spectral signatures of four charcoal samples (solid curves) and of three vegetation samples (dot-dashed curves). Gray boxes delimit the SWIR (between 2.0 and 2.5  $\mu\text{m}$ ) and MIR (between 3.5 and 4  $\mu\text{m}$ ) spectral regions in order to emphasize their contrast. Charcoal and vegetation signatures were respectively obtained from samples of fire residues from Alta Floresta, state of Mato Grosso, Brazil and from the Advanced Spaceborne Thermal Emission and Reflection Radiometer (ASTER) spectral library (Baldridge et al., 2009).

spectral signatures, in contrast with temperate and boreal regions, where one may wait until the end of the fire season to map scars from previous months (Pereira, 2003). This procedure is not feasible in tropical savannas, where combustion products are easily scattered by wind, and the charcoal spectral signal quickly fades out. Burning of converted tropical forest produces a short-lived signal, since fire in this region is closely related to pasture and agriculture practices, which disturb the soil surface. In tropical regions, mapping burned areas with remote sensing data has, therefore, to be performed during the dry season, i.e. simultaneously with the fire episodes. Results will be, in general, largely affected by smoke aerosols, which contaminate surface observation and reduce the spectral contrast between distinct land cover types. According to Kaufman (1995), most of these particles may remain in the atmosphere for around a week. In addition, from July to October, i.e. during the Amazon fire season, a large high pressure system tends to dominate the region, inhibiting precipitation and reducing relative humidity due to the subsidence of dry air from the upper levels of the atmosphere (Nobre et al., 1998). The associated atmospheric circulation favors the retention over a large horizontal area of smoke emitted by fires, reducing visibility to the point of closing airports during, even up to two or three weeks after the end of the fire season (Reinhardt et al., 2001).

Under such circumstances, the MIR spectral band appears especially adequate for monitoring the land surface during fire episodes, because it is largely unaffected by the presence of most aerosols. This feature of MIR becomes well apparent when atmospheric transmittance attenuation is computed over the visible (VIS) to MIR bands, for different levels of smoke contamination due to biomass burning. Transmittance attenuation is defined here as the difference between the transmittance from an aerosol-free atmosphere and that from an atmosphere with a given level of smoke contamination. Fig. (2) shows the impact on MODIS VIS to MIR channels resulting from increasing the aerosol optical depth (AOD) associated to biomass burning. Values of transmittance attenuation were obtained from radiative transfer simulations performed with MODTRAN-4 (see Section 3.3). The model was run using a Tropical atmospheric profile (see Table 2) perturbed with aerosols associated to biomass burning, based on cloud-screened level 2.0 AOD at 440 nm ( $\tau_a(0.44)$ ) data from the Abracos Hill station. The station is located in Rondonia, Brazil, an area with high fire activity and is part of the

Aerosol Robotic Network (AERONET), a global sun/sky radiometer network for aerosol monitoring (Holben et al., 1998).

During the dry season, in an atmosphere heavily contaminated by smoke (e.g. with an AOD at 0.44  $\mu\text{m}$  for about 2.73), the VIS and NIR channels (0.4–1.0  $\mu\text{m}$ ) are inadequate for surface observation. Even at lower levels of contamination by smoke (with an AOD at 0.44  $\mu\text{m}$  lower than 0.72) VIS channels remain strongly affected. Although less sensitive to smoke aerosol, atmospheric transmittance in the SWIR (1.2–2.5  $\mu\text{m}$ ) spectral region is still markedly attenuated. In striking contrast, the MIR domain is practically unaffected by smoke, allowing for almost undisturbed surface observation. The atmospheric transmittance attenuation displays almost constantly low values of atmospheric contamination by smoke in all three cases analyzed, including under extreme AOD conditions. This is a major reason to favor the MIR spectral domain for monitoring and mapping burned areas.

### 3. Data and methods

#### 3.1. Theoretical background

Top of the atmosphere (TOA) radiance measured by a sensor in the MIR region results from the contribution of the reflective and thermal emissive components. In case of clear sky conditions, radiation balance is translated by the so-called radiative transfer equation (RTE):

$$L_{\text{MIR}} = t_{\text{MIR}} \rho_{\text{MIR}} \frac{E_{\text{OMIR}}}{\pi} \mu_0 + \tau_{\text{MIR}} \varepsilon_{\text{MIR}} B(\lambda_{\text{MIR}}, T_s) + \tau_{\text{MIR}} \rho_{\text{MIR}} \bar{L}_{\text{atm}, \text{MIR}} \downarrow + L_{\text{atm}, \text{MIR}} \uparrow + L_s \quad (1)$$

In the previous equation  $t_{\text{MIR}}$  is the two-way atmospheric transmittance (sun–surface–sensor);  $\rho_{\text{MIR}}$  is the surface reflectance;  $E_{\text{OMIR}}$  is the exo-atmospheric irradiance;  $\mu_0$  is the cosine of the solar zenith angle (SZA);  $\tau_{\text{MIR}}$  is the one-way atmospheric transmittance (surface–sensor);  $\varepsilon_{\text{MIR}}$  is the surface emissivity;  $B(\lambda_{\text{MIR}}, T_s)$  is the emitted radiance given by Planck's function for surface temperature  $T_s$  and central wavelength  $\lambda_{\text{MIR}}$ ;  $\bar{L}_{\text{atm}, \text{MIR}} \downarrow$  is the hemispherical average of the atmospheric downward emission; and  $L_{\text{atm}, \text{MIR}} \uparrow$  is the atmospheric upward emission; and  $L_s$  is the term associated with atmospheric scattering.

The first term on the right-hand side of Eq. (1) represents the solar radiance that is attenuated by the atmosphere in its downward path, then reflected by the surface and again attenuated in its upward path to the sensor. The second term represents the radiance emitted by the surface that is attenuated by the atmosphere. The third term denotes the downward atmospheric radiance that is reflected by the surface and then attenuated in its upward path to the sensor. The fourth term represents the radiance emitted by the atmosphere towards the sensor. The last term is associated with atmospheric scattering.

Since the Earth surface is opaque and assuming it behaves as a Lambertian emitter–reflector, surface reflectance and emissivity are related as:

$$\rho_{\text{MIR}} = 1 - \varepsilon_{\text{MIR}} \quad (2)$$

Using Eq. (2) and neglecting the atmospheric scattering term,  $L_s$ , the solution to Eq. (1) is given by:

$$\rho_{\text{MIR}} = \frac{L_{\text{MIR}} - \tau_{\text{MIR}} B(\lambda_{\text{MIR}}, T_s) - L_{\text{atm}, \text{MIR}} \uparrow}{t_{\text{MIR}} \frac{E_{\text{OMIR}}}{\pi} \mu_0 - \tau_{\text{MIR}} B(\lambda_{\text{MIR}}, T_s) + \tau_{\text{MIR}} \bar{L}_{\text{atm}, \text{MIR}} \downarrow} \quad (3)$$

#### 3.2. Retrieval of MIR reflectance

Eq. (3) lays the grounds for the so-called physically-based methods, which involve a direct evaluation of all constituents of the MIR signal by means of a radiative transfer model, requiring

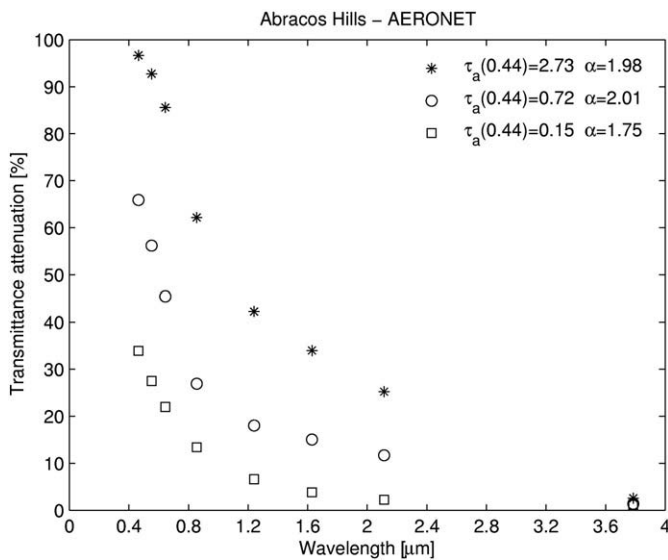


**Fig. 2.** Atmospheric transmittance attenuation [%] on MODIS VIS to MIR channels for three different levels of smoke contamination due to biomass burning.  $\tau_a(0.44)$  indicates the AOD at 0.44  $\mu\text{m}$  and  $\alpha$  denotes the Ångström parameter, which characterizes aerosol particle size distribution.

substantial computational means. Operational use of physically-based methods is limited by other factors, namely the need of quantitative information on atmospheric conditions, mainly humidity and temperature profiles, in order to perform the atmospheric corrections.

The above-mentioned limitations led to the development of simpler methods, like the one proposed by KR94, which require neither direct knowledge of atmospheric conditions, nor a radiative transfer model. The approach is based on the studies of Gesell (1989) and Ruff and Gruber (1983), who pointed out the existence of a mutual compensation between attenuation and thermal emission terms, so that both atmospheric transmittances (i.e.  $t_{\text{MIR}}$  and  $\tau_{\text{MIR}}$ ) may be assumed as equal to unity, and both the atmospheric downward and upward thermal emission terms may be neglected. The validity of these assumptions may be assessed by simplifying Eq. (3) and then justifying the performed simplifications using typical values of the relevant terms of Eq. (3) for surface and atmospheric conditions associated to dense, dark vegetation areas in mid-latitude environments. Typical values are given in Table 1 for nadir view and three different values of SZA, respectively 0, 15 and 45°, where a Mid-Latitude Winter atmospheric profile (see Table 2) and a surface temperature  $T_s$  of 290 K are assumed. Accordingly, after some algebraic manipulations, Eq. (3) may be rewritten as:

$$\rho_{\text{MIR}} = \frac{L_{\text{MIR}} - B(\lambda_{\text{MIR}}, T_s) - \Delta_1}{\left[ \frac{E_{\text{OMIR}}}{\pi} \mu_0 - B(\lambda_{\text{MIR}}, T_s) \right] [1 + \Delta_2]} \quad (4)$$

where:

$$\Delta_1 = (\tau_{\text{MIR}} - 1)B(\lambda_{\text{MIR}}, T_s) + L_{\text{atm,MIR}} \uparrow \quad (5)$$

$$\Delta_2 = \frac{(\tau_{\text{MIR}} - 1) \frac{E_{\text{OMIR}}}{\pi} \mu_0 - (\tau_{\text{MIR}} - 1)B(\lambda_{\text{MIR}}, T_s) + \tau_{\text{MIR}} \bar{L}_{\text{atm,MIR}} \downarrow}{\frac{E_{\text{OMIR}}}{\pi} \mu_0 - B(\lambda_{\text{MIR}}, T_s)} \quad (6)$$

Since  $\Delta_2 \ll 1$  according to the values in Table 1, the factor  $1/(1 + \Delta_2)$  in Eq. (4) may be expanded in a Taylor series up to the first order leading to:

$$\rho_{\text{MIR}} = \frac{L_{\text{MIR}} - B(\lambda_{\text{MIR}}, T_s) - \Delta_1}{\left[ \frac{E_{\text{OMIR}}}{\pi} \mu_0 - B(\lambda_{\text{MIR}}, T_s) \right]} [1 + \Delta_2]. \quad (7)$$

Taking further into account that  $\Delta_1 \ll L_{\text{MIR}} - B(\lambda_{\text{MIR}}, T_s)$ , terms  $\Delta_1$  and  $\Delta_2$  may be neglected in Eq. (7) leading to the following simplified form:

$$\rho_{\text{MIR}} = \frac{L_{\text{MIR}} - B(\lambda_{\text{MIR}}, T_s)}{\frac{E_{\text{OMIR}}}{\pi} \mu_0 - B(\lambda_{\text{MIR}}, T_s)}. \quad (8)$$

The above described mathematical procedure may be also viewed from a physical point of view. First, consider the numerator of the second hand term of Eq. (3), and suppose the atmospheric upward emission term ( $L_{\text{atm,MIR}} \uparrow$ ) is neglected. Since  $L_{\text{MIR}}$  is fixed, the only way to compensate the neglected term is by increasing the contribution of the remaining term,  $\tau_{\text{MIR}}B(\lambda_{\text{MIR}}, T_s)$ . This is only possible by increasing the atmospheric transmittance  $\tau_{\text{MIR}}$ , in particular by setting it equal to unity. Now, taking into consideration

**Table 2**

Effects of water vapor content [ $\text{g cm}^{-2}$ ] on atmospheric terms for the three profiles analyzed, considering nadir view and a SZA of 0°.

Profile	Water vapour content [ $\text{g cm}^{-2}$ ]	$\tau_{\text{MIR}}$	$t_{\text{MIR}}$	$L_{\text{atm,MIR}} \uparrow$ [ $\text{W m}^{-2} \mu\text{m}^{-1} \text{sr}^{-1}$ ]	$\bar{L}_{\text{atm,MIR}} \downarrow$ [ $\text{W m}^{-2} \mu\text{m}^{-1} \text{sr}^{-1}$ ]
MLW	0.85	0.91	0.81	0.006	0.012
MLS	2.92	0.83	0.70	0.038	0.068
TRO	4.11	0.79	0.65	0.057	0.104

the denominator, suppose the atmospheric downward emission term ( $\bar{L}_{\text{atm,MIR}} \downarrow$ ) is neglected. Then, in order to compensate the neglected term, either the contribution of term  $\tau_{\text{MIR}}B(\lambda_{\text{MIR}}, T_s)$ , or the contribution of term  $t_{\text{MIR}} \frac{E_{\text{OMIR}}}{\pi} \mu_0$  have to be increased. However, the first possibility is ruled out by the fact that it was already assumed that  $\tau_{\text{MIR}} = 1$ . Therefore, the contribution of the  $t_{\text{MIR}} \frac{E_{\text{OMIR}}}{\pi} \mu_0$  term has to be raised by increasing  $t_{\text{MIR}}$ , in particular by setting it equal to unity. Setting both  $t_{\text{MIR}}$  and  $\tau_{\text{MIR}}$  to unity does lead to the required increase that compensates for neglecting the  $\bar{L}_{\text{atm,MIR}} \downarrow$  term. This is due to the fact that, in general,  $t < \tau$  and therefore the assumption  $t_{\text{MIR}} = \tau_{\text{MIR}} = 1$  leads to a greater increase in the contribution of  $t_{\text{MIR}} \frac{E_{\text{OMIR}}}{\pi} \mu_0$  term than in  $\tau_{\text{MIR}}B(\lambda_{\text{MIR}}, T_s)$  term.

KR94 introduced another approximation for Eq. (8), that consists of using the brightness temperature,  $T_{\text{B,TIR}}$ , from a thermal infrared (TIR) band (10–12  $\mu\text{m}$ ) as a surrogate for the land surface temperature (LST),  $T_s$ . In fact, as pointed out by Prata et al. (1995), brightness temperature is usually lower than surface temperature, the difference typically ranging from 1 to 5 K in TIR.

Following a procedure similar to the one above-described, Eq. (8) may be approximated (up to the first order) as:

$$\rho_{\text{MIR}} = \frac{L_{\text{MIR}} - B(\lambda_{\text{MIR}}, T_{\text{B,TIR}}) - \Delta_3}{\frac{E_{\text{OMIR}}}{\pi} \mu_0 - B(\lambda_{\text{MIR}}, T_{\text{B,TIR}})} \left[ 1 - \frac{\Delta_3}{\frac{E_{\text{OMIR}}}{\pi} \mu_0 - B(\lambda_{\text{MIR}}, T_{\text{B,TIR}})} \right]. \quad (9)$$

Since, according to results in Table 1,  $\Delta_3 = B(\lambda_{\text{MIR}}, T_s) - B(\lambda_{\text{MIR}}, T_{\text{B,TIR}}) \ll L_{\text{MIR}} - B(\lambda_{\text{MIR}}, T_{\text{B,TIR}})$  and  $\frac{\Delta_3}{\frac{E_{\text{OMIR}}}{\pi} \mu_0 - B(\lambda_{\text{MIR}}, T_{\text{B,TIR}})} \ll 1$ , Eq. (3) may be approximated by the following equation, that represents the final form of the KR94 algorithm:

$$\rho_{\text{MIR}} = \frac{L_{\text{MIR}} - B(\lambda_{\text{MIR}}, T_{\text{B,TIR}})}{\frac{E_{\text{OMIR}}}{\pi} \mu_0 - B(\lambda_{\text{MIR}}, T_{\text{B,TIR}})}. \quad (10)$$

### 3.3. Radiative transfer simulations

As pointed out in the Introduction, the aim of the present paper is to perform a systematic assessment of the performance of the KR94 algorithm when applied to burned area discrimination under a wide range of atmospheric, surface and geometry conditions, paying special attention to those expected when applying the algorithm to the Amazon and “cerrado” regions.

For this purpose, estimation of the error associated with MIR reflectance as retrieved using Eq. (10) will be performed based on a

**Table 1**

Typical values of the different terms of Eq. (3) in the case of nadir view and for three different SZA considering a Mid-Latitude Winter atmospheric profile and a surface temperature,  $T_s$ , equal to 290 K.

SZA	$\tau_{\text{MIR}}$	$t_{\text{MIR}}$	$L_{\text{MIR}}^a$	$B(\lambda_{\text{MIR}}, T_s)^a$	$B(\lambda_{\text{MIR}}, T_{\text{B,TIR}})^a$	$L_{\text{atm,MIR}} \uparrow^a$	$\frac{E_{\text{OMIR}}}{\pi} \mu_0^a$	$\bar{L}_{\text{atm,MIR}} \downarrow^a$
45°	0.912	0.794	0.700	0.315	0.212	0.006	2.46	0.011
15°	0.912	0.813	0.872	0.315	0.212	0.006	3.29	0.011
0°	0.912	0.816	0.899	0.315	0.212	0.006	3.42	0.011

<sup>a</sup> [ $\text{W m}^{-2} \mu\text{m}^{-1} \text{sr}^{-1}$ ].



large number of simulated top of atmosphere (TOA) radiances. These simulations are generated with MODTRAN-4, a widely used radiative transfer model (Berk et al., 2000) encompassing a large set of observation conditions. The simulations are performed in the spectral ranges of  $3.62\text{ }\mu\text{m}$ – $3.97\text{ }\mu\text{m}$  and  $10\text{ }\mu\text{m}$ – $12\text{ }\mu\text{m}$ , i.e. covering MODIS channels 20 and 31. Brightness temperature from MODIS channel 31 is also required as input to Eq. (10).

The atmospheric contribution is computed for three geographical-seasonal model atmospheres stored in MODTRAN-4, namely Mid-Latitude Winter (MLW), Mid-Latitude Summer (MLS), and Tropical (TRO). Use of mid-latitude profiles (i.e. MLW and MLS) is required to establish a baseline of performance of KR94 when subject to atmospheric, surface and geometric conditions for which the algorithm was specifically designed. Such baseline will then serve to assess the limitations of KR94 when employed beyond specifications, namely in case of tropical environments (e.g. as described by the TRO profile).

The three standard atmospheres cover a wide range of atmospheric conditions, with water vapor content of 0.85, 2.92 and  $4.11\text{ g cm}^{-2}$  and 2-m air temperature ( $T_{\text{atm}}$ ) of 272.2, 294.2 and 299.7 K, for MLW, MLS, and TRO respectively. The assigned LST values are based on the 2-m air temperature of each profile, varying from  $T_{\text{atm}}$  to  $T_{\text{atm}} + 30.0\text{ K}$  in steps of 1.0 K, totalizing 31 different values. The sun-view geometry consists of 31 solar zenith angles, from  $0^\circ$  to  $60^\circ$  in steps of  $2^\circ$ , and of a single view zenith angle of  $0^\circ$ . Although nadir viewing is limited along the tropics when using polar orbiting instruments (such as MODIS), choice of a nadir view corresponds to the most favorable surface observation conditions. If problems arise when simulating nadir viewing (i.e. the most favorable case), then performance is expected to degrade for less favorable observation conditions. In fact, simulations were also performed for off-nadir viewing angles and, as expected, results (not shown) revealed a slight degradation in performance of the KR94 algorithm with increasing viewing angle, a feature consistent with former studies (França &

Setzer, 1998; Jiang et al., 2006) that demonstrate weak dependence of MIR region on view angle variations.

The ranges of SZA and LST are set to be representative of the observed geometric and surface conditions characteristic of regions associated to each atmospheric profile. For instance, Fig. 3 depicts pixel values of the third quartile (P75) of LST during August 2008, retrieved over Brazil using the Spinning Enhanced Visible and Infra-Red Imager (SEVIRI) on-board METEOSAT-8. Fig. 4 presents monthly P75 values, throughout the year, of SZA as obtained from a large sample of pixels from MODIS imagery that has been operationally used for burned area discrimination over Brazil. During the fire season (from June to October) very high values of LST are observed over Amazonia and especially over the adjacent “cerrado”, region, where a large area may be found that presents values of P75 larger than 320 K. In addition, more than 25% of the pixels are associated to values of SZA greater than  $40^\circ$ , i.e. to low values of the solar signal.

Two types of surface cover were considered, namely burned and unburned. Both surface types were assumed to be homogeneous and Lambertian, the burned and unburned surfaces being characterized respectively by charcoal and vegetation spectra. Spectral libraries like ASTER and MODIS-UCSB supply reliable reflectance data for different types of materials, such as vegetation, water, soil, rocks and man-made. However, to the best of our knowledge, no reflectance measurements are currently available for charcoal, ash or any burned plant material, in the spectral region accounted for in this study. Therefore, four fire residue samples were collected at Alta Floresta, state of Mato Grosso, Brazil. Charcoal spectra were measured at the NASA Jet Propulsion Laboratory and may be viewed as typical of tropical environments. Mean values of the four charcoal spectra were then used to prescribe the surface reflectance of the burned surface as input to MODTRAN-4. Regarding the unburned surface, prescribed reflectance values were obtained from a set of 25 surfaces from the MODIS-UCSB spectral library. The set includes most vegetation types

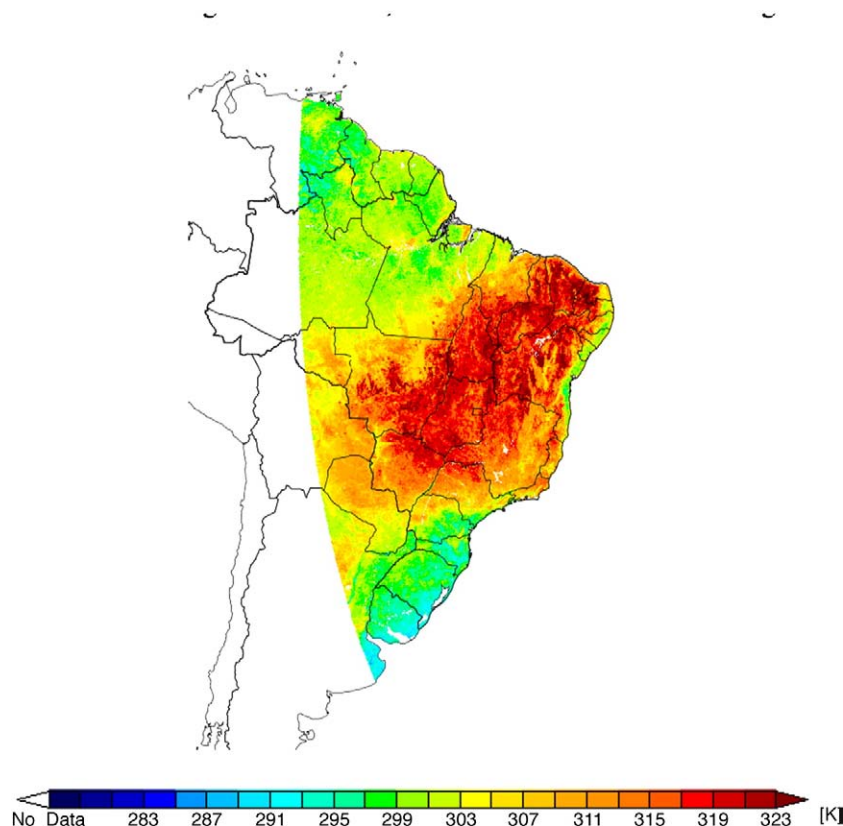
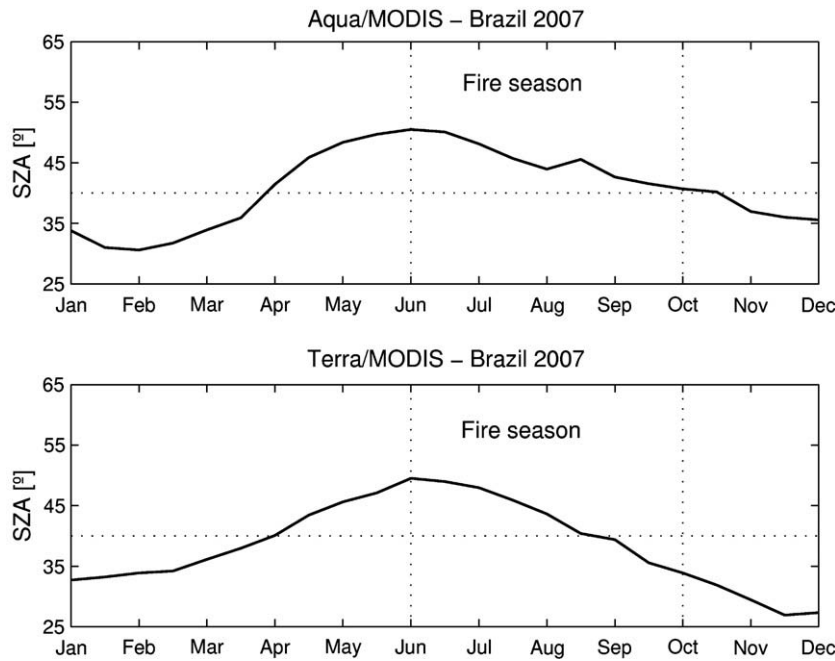


Fig. 3. Monthly values of P75 of LST during August, 2008 over Brazil. Data were retrieved from METEOSAT-8/SEVIRI data.



**Fig. 4.** Monthly values of P75 of SZA as obtained from samples of AQUA/MODIS and TERRA/MODIS imagery along the year of 2007 over Brazil. The threshold of 40° for SZA is highlighted by the dotted horizontal line. Dotted vertical lines delimit the fire season in Amazonia (June to October).

(Salisbury & D'Aria, 1994; Peres & DaCamara, 2004), with reflectance values varying from 0.01 to 0.04, in the MIR region. A value of 0.24 (0.03) was, accordingly, prescribed for MIR reflectance for the burned (unburned) types of surface cover. These values were obtained by averaging the MIR spectral signature for the four (25) considered charcoal (vegetation) types, which were convolved with the MODIS channel 20 normalized response function. Results ought to be applicable to other sensors having spectral windows similar to that used in this work.

## 4. Analysis and results

### 4.1. MODTRAN-4 simulations

As discussed in the previous section, the method developed by KR94 relies on a number of simplifying assumptions regarding atmospheric transmittances and atmospheric downward and upward thermal emission radiances. All these terms are correlated and depend essentially on atmospheric water vapor content. When atmospheric water vapor increases, atmospheric transmittances decrease, whereas the atmospheric downward and upward thermal emission radiances increase. Table 2 shows the range of atmospheric terms that may typically be found in the MIR region, in the case of the three geographical-seasonal model atmospheres considered, i.e., when varying from 'dry' to 'moist' conditions. For instance, whereas high transmittances and low path-radiances values characterize the MLW atmospheric profile, the TRO profile is associated to lower transmittances and relatively high path-radiance values. It is therefore to be expected that use of Eq. (10) in retrieving MIR reflectance may introduce systematic deviations, especially in the case of 'moist' atmospheres. For example, in the case of TRO, the relative error associated to the assumption of  $\tau_{\text{MIR}} = 1$  (instead of the realistic value  $\tau_{\text{MIR}} = 0.79$ ) is about 27% but drops to 10% in the case of MLW (taking into account that  $\tau_{\text{MIR}} = 0.91$ ). In the case of the two-way atmospheric transmittance, the relative error associated to the assumption of  $t_{\text{MIR}} = 1$  (instead of  $t_{\text{MIR}} = 0.65$ ) in the case of TRO is about 54% but drops to 24% in the case of MLW (where  $t_{\text{MIR}} = 0.81$ ). In a similar fashion, neglecting the atmospheric downward emission term leads

to a relative error of 17% for the TRO profile, in contrast with MLW where the corresponding error decreases to 3%. Finally, neglecting the atmospheric upward emission term leads to a relative error of 9% for the TRO profile and just to an error of 2% in the case of MLW.

Accuracy of the solutions provided by Eq. (10) may be assessed by evaluating the corresponding relative errors, defined as the differences between retrieved values using Eq. (3) and the corresponding prescribed values as input to MODTRAN-4, divided by the latter values. Figs. 5–7 present the obtained values of relative errors of MIR reflectance as a function of LST and SZA. The curves correspond to nadir viewing conditions and represent charcoal (left panels) and vegetation (right panels) surfaces for MLW (Fig. 5), MLS (Fig. 6) and TRO (Fig. 7). It is worth stressing that ranges of LST considered are different for each profile (as discussed in Section 3.3) and reflect the surface conditions typically associated to each type of atmosphere.

It is well apparent that relative errors strongly depend on the surface type, for all three atmospheric profiles. In particular, it may be noted that the magnitude of relative errors is considerably larger for vegetation than for charcoal, and increases with moisture content, MLW showing the lowest values and TRO the highest. For instance, the lower values obtained in the case of MLW are in close agreement with results found by KR94, who estimated the accuracy of Eq. (10) to lie in the range of 0.01–0.02 (absolute errors) for a mid-latitude atmosphere and for the range of reflectance to be expected from a variety of vegetation and soils (0.01–0.06). In strong contrast, vegetation surfaces present extremely large relative errors, ranging from 100% to 1200% for LST values to be expected in tropical regions. Taking the value of 0.03 as reference for reflectance of vegetation, the obtained range corresponds to absolute errors of 0.06–0.4. In the case of charcoal, relative errors are one order of magnitude smaller, ranging from –20%–80%, i.e. from about –0.05–0.2 in terms of absolute error, and taking a reference value of 0.24 for charcoal reflectance. Dependence of the relative error on LST is stronger than on SZA, especially for values of SZA lower than 30°, a feature clearly revealed by the low slope of the error curves in Figs. 5–7.

Performance of the KR94 algorithm is closely linked to the magnitude of the relative contribution of thermal emitted radiance,  $L_e$ , to the total TOA MIR radiance,  $L_{\text{MIR}}$ , given by Eq. (1). It may be

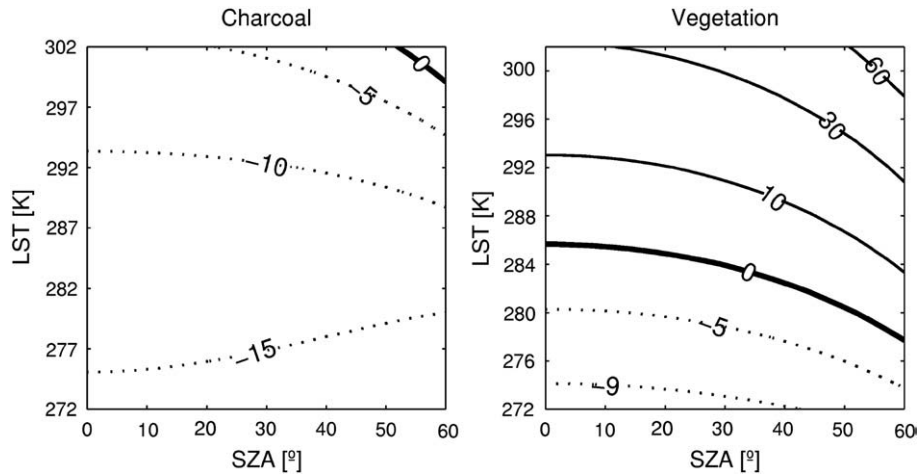


**Fig. 5.** Relative error [%] on MIR reflectance (retrieved minus prescribed values) as a function of LST and SZA in the case of MLW profile for charcoal (left panel) and vegetation (right panel) surfaces. Solid (dotted) curves indicate positive (negative) errors and the thick curve highlights the no-error line.

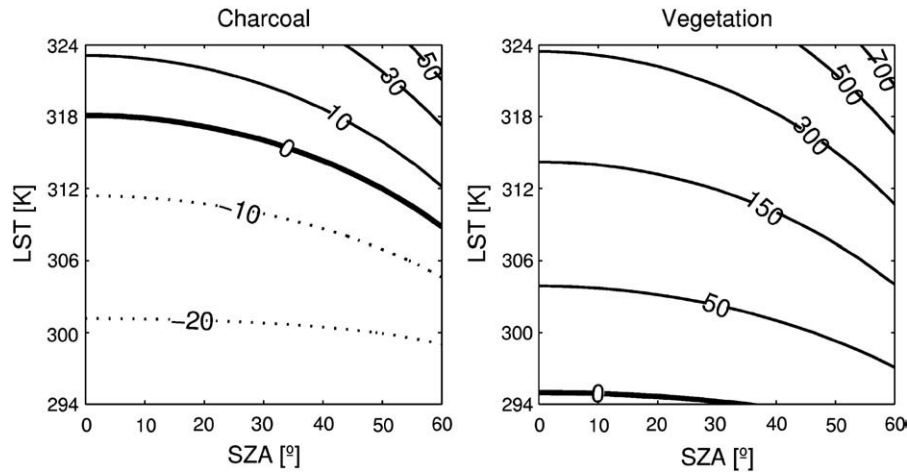


**Fig. 6.** As in Fig. 5 but in the case of MLS.

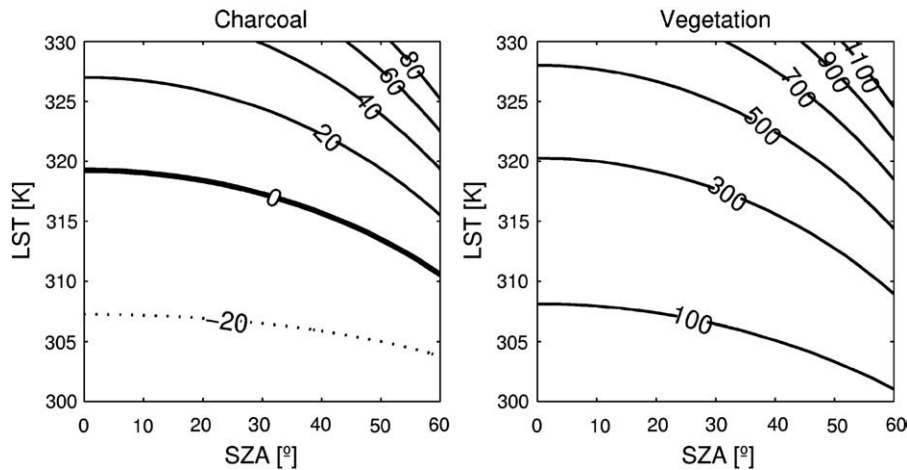


**Fig. 7.** As in Fig. 5 but in the case of TRO.

noted that  $L_e$  is given by the second, third and fourth terms of the right-hand side of Eq. (1), i.e.

$$L_e = \tau_{\text{MIR}} \epsilon_{\text{MIR}} B(\lambda_{\text{MIR}}, T_s) + \tau_{\text{MIR}} \rho_{\text{MIR}} \bar{L}_{\text{atm}, \text{MIR}} \downarrow + L_{\text{atm}, \text{MIR}} \uparrow. \quad (11)$$

When the ratio  $L_e/L_{\text{MIR}}$  exceeds a threshold of about 0.75 the solutions provided by Eq. (10) are contaminated by unacceptably large relative errors, on the order of 100%. The magnitude of  $L_e/L_{\text{MIR}}$ , and therefore the range of validity of Eq. (10), mainly depends on the type of the surface considered, as well as on its temperature,

atmospheric profile, and sun elevation angle. Fig. 8 presents the dependence of  $L_e/L_{MIR}$  on LST for vegetation (circles) and charcoal (squares) under two extreme illumination angles, respectively an SZA of  $0^\circ$  (open symbols) and of  $60^\circ$  (black symbols), and for the two extreme cases of atmospheric moisture content, respectively MLW (left panel) and TRO (right panel) profiles. The contrasting behavior of charcoal and vegetation is well apparent. In the case of charcoal, high values of MIR reflectance (about 0.24) lead to a major contribution of the reflected component and, therefore, the ratio  $L_e/L_{MIR}$  will be below 50% (75%) in the case of MLW (TRO), except for large values of LST, above 289 K (293 K) for MLW (TRO), associated to very low sun elevation angles (SZA =  $60^\circ$ ). Acceptable estimates of charcoal reflectance are therefore to be expected from Eq. (10), the sole exception being cases of high LST values (larger than 320 K), co-occurring with high SZA values (larger than  $50^\circ$ ), which may lead to relative errors in excess of 25%. Because of the very low vegetation reflectance (about 0.03, i.e. eight times lower than that of charcoal), total TOA MIR radiance,  $L_{MIR}$ , will be primarily due to the thermal emitted component, and a deeply contrasting behavior is to be expected between charcoal and vegetation. In the latter type of surface, the ratio  $L_e/L_{MIR}$  is always larger than 75% in the case of TRO, and in the case of MLW for low solar elevation (SZA =  $60^\circ$ ). Even for solar zenith conditions (SZA =  $0^\circ$ ) the ratio  $L_e/L_{MIR}$  exceeds 75% in the case of MLW, for LST values as low as 288 K. Implications of the solutions provided by Eq. (10) on relative errors are well depicted in the left panels of Figs. 5 and 7; in the case of TRO, relative errors are unacceptably large (exceeding 50%) over the entire domain considered, whereas in the case of MLW relative errors are larger than 25% for values of LST beyond 290 K, whenever SZA surpasses  $50^\circ$ .

The above-discussed limitations of the KR94 algorithm may give rise to serious difficulties when attempting to discriminate between burned and unburned surfaces, in particular in the case of tropical environments. For instance, an absolute error of 0.2 in a typical vegetation reflectance of about 0.03 leads to a retrieved value of about

0.23 which reaches the range characteristic of charcoal. The problem is illustrated in Fig. 9, which presents results obtained when using Eq. (10) to retrieve the reflectance of vegetation (with the prescribed value of 0.03) and of charcoal (with the prescribed value of 0.24) in the three considered cases of MLW, MLS and TRO, for values of SZA from 0 to  $60^\circ$  and for ranges of typical values of LST for each profile. It is well apparent that the accuracy of retrieved values of reflectance is much more sensitive to LST and SZA in the case of vegetation than for charcoal. For instance, the reference contour line of 0.03 (for vegetation) is displaced out of the considered domain in the case of MLS and TRO and, even for MLW, it is located at the bottom, almost out of the domain. The displacement of the reference contour line of 0.24 for charcoal is much smaller and is barely noticeable in the case of MLW. However, the robustness of Eq. (10) in the case of charcoal is not enough to discriminate burned from unburned surfaces, because values of reflectance for vegetation attain those characteristics of charcoal for sufficiently high values of LST and SZA. As shown in Fig. 9, in the case of MLS, even if the discontinuities observed along the band separating the two considered surfaces indicate the possibility of discriminating between them, values of the contour lines on both sides are larger than 0.20. Therefore, it is not possible to label either type as the unburned surface. The situation is even worse for TRO where, for values of LST greater than 315 K and SZA larger than  $30^\circ$ , both surfaces reach similar reflectance values, becoming undistinguishable.

#### 4.2. Case study

A more realistic assessment of the implications of using Eq. (10) for burned area discrimination in tropical environments may be achieved by means of a case study based on satellite imagery. However, as pointed out by Roger and Vermote (1998), any attempt to validate retrieved values of MIR reflectance from satellite data is virtually impaired by the absence of “in-situ” (direct) measurements. This limitation may be circumvented by creating a reference dataset of

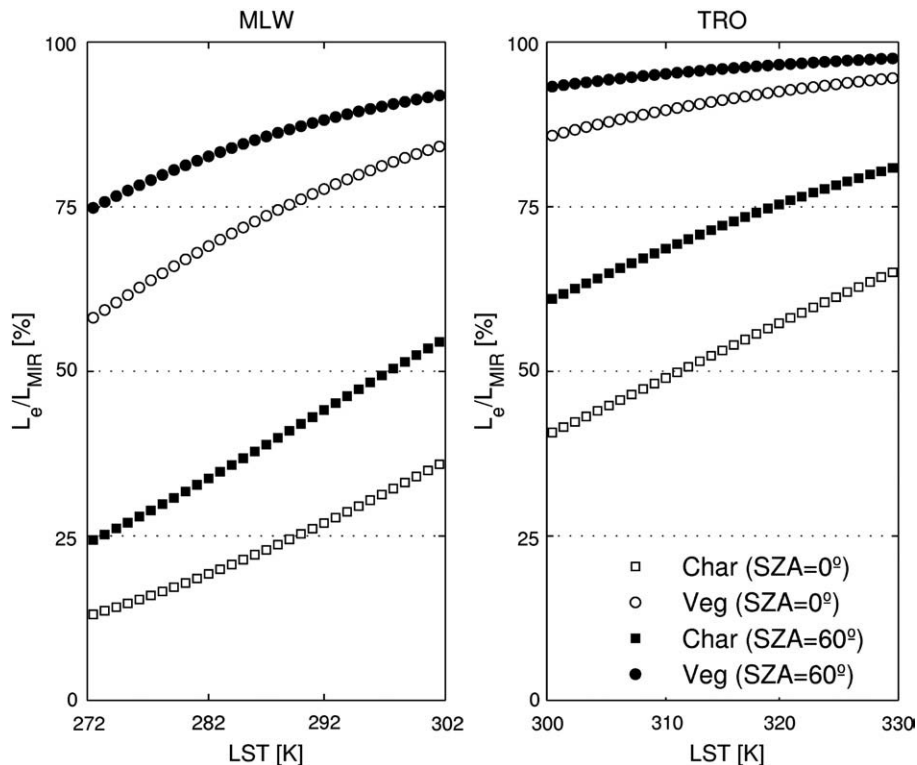
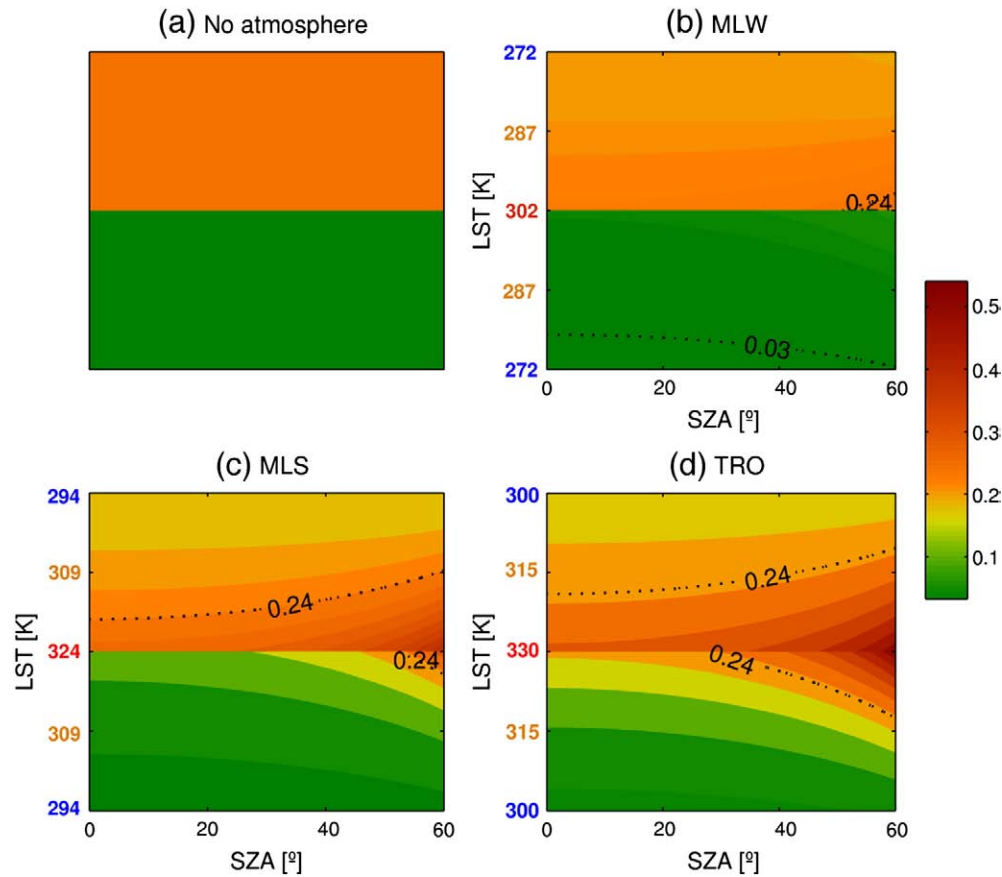


Fig. 8. Plot of the ratio  $L_e/L_{MIR}$  [%] as a function of LST in the case of MLW (left panel) and TRO (right panel). Square (circle) symbols denotes charcoal (vegetation) surface whereas open (black) symbols characterizes SZA of  $0^\circ$  ( $60^\circ$ ).





**Fig. 9.** Diagram of values of reflectance for vegetation and charcoal surfaces for different atmospheric profiles, LST and SZA; a) the two surfaces with prescribed constant values of 0.03 and 0.24 for vegetation (green) and charcoal (orange); b) to d) retrieved values of reflectance using Eq. (10) as a function of SZA and LST for MLW, MLS and TRO profiles.

MIR reflectance based on information from a real satellite image. The adopted approach consists of the following steps: (1) collect information about land surface temperature, land surface emissivity, atmospheric profiles and view/solar angles for the selected scene; (2) use a radiative transfer model (MODTRAN-4 in the present study) to compute the respective values of transmittance and atmospheric parameters; and (3) use Eq. (3) with values obtained in the previous steps to retrieve MIR reflectance from the total signal. The generated reference dataset of MIR reflectance may then be used to validate the corresponding MIR reflectance as retrieved by means of KR94.

Taking into account the described procedure, it seems appropriate to select an image where the atmospheric conditions are particularly favorable, e.g. with low values of the water vapor column, and a low amount of aerosols (i.e. with a clear sky surrounding). Since results from simulations (Section 4.1) showed that the accuracy of retrieved values of reflectance is very sensitive to high values of LST, it seems also appropriate to select an image with moderate values of LST.

All the above-mentioned favorable characteristics are met in the case of the large fire event that took place from April 30 to May 12, 2006 and affected the entire area of the Ilha Grande National Park, located between the states of Paraná and Mato Grosso do Sul, Brazil. The burned is about 200 km<sup>2</sup>, as estimated by INPE based on information from LANDSAT TM imagery (Fig. 10). A total of 413 active fires during the above-mentioned period were also identified by INPE, using data from GOES, NOAA, Aqua and Terra satellites.

Performance of Eq. (10) was assessed using TOA values of MIR radiance and TIR brightness temperature as acquired on May 12, 2006 by the MODIS instrument on-board Aqua. Data were obtained from the Aqua/MODIS Level 1B 1 km V5 product, MYD021 (MCST, 2006) and

correspond to channels 20 (centered at 3.785  $\mu\text{m}$ ) and 31 (centered at 11.017  $\mu\text{m}$ ). Surface values of MIR reflectance were then retrieved by solving Eq. (3) using MODTRAN-4, using information about surface temperature and sun elevation together with data of temperature and humidity for the atmospheric column. Pixels values of LST and of SZA, varying from 295 to 315 K and from 48.5 to 51°, respectively were obtained from Land Surface Temperature/Emissivity Daily 5-Min L2 Swath 1 km product, MYD11\_L2 (Wang, 1999). Atmospheric profiles of temperature and humidity were obtained from the Atmosphere Profile Level 2.0 product, MYD07\_L2 (Seemann et al., 2006), the water vapor content over the selected area varying from 1.3 to 2.3 g cm<sup>-2</sup>, a quite low amount when compared with the value of 4.11 g cm<sup>-2</sup> of the TRO profile stored in MODTRAN-4. Fig. 11 represents the MODIS mean profiles of temperature and humidity together with the TRO profile that will be used to generate synthetic imagery with characteristics to be expected over tropical environments.

Retrieved values of surface MIR reflectance and values of LST are shown in Fig. 12. Higher values of MIR reflectance and LST over the burned area are particularly conspicuous, especially because of the contrasting behavior of the surrounding vegetated areas, which present a large spatial variability of reflectance and temperature.

Values of retrieved surface MIR reflectance and of LST (Fig. 12) were input to MODTRAN-4, to produce synthetic images of TOA MIR radiance and TIR brightness temperature. These images correspond to the following two environments, characterized by atmospheric and surface conditions expected in tropical regions; i) the TRO environment, obtained using the TRO profile and the LST of May 12, 2006 and ii) the TRO-HOT environment, obtained using the TRO profile and LST + 20 K. The KR94 algorithm was then used to retrieve values of surface

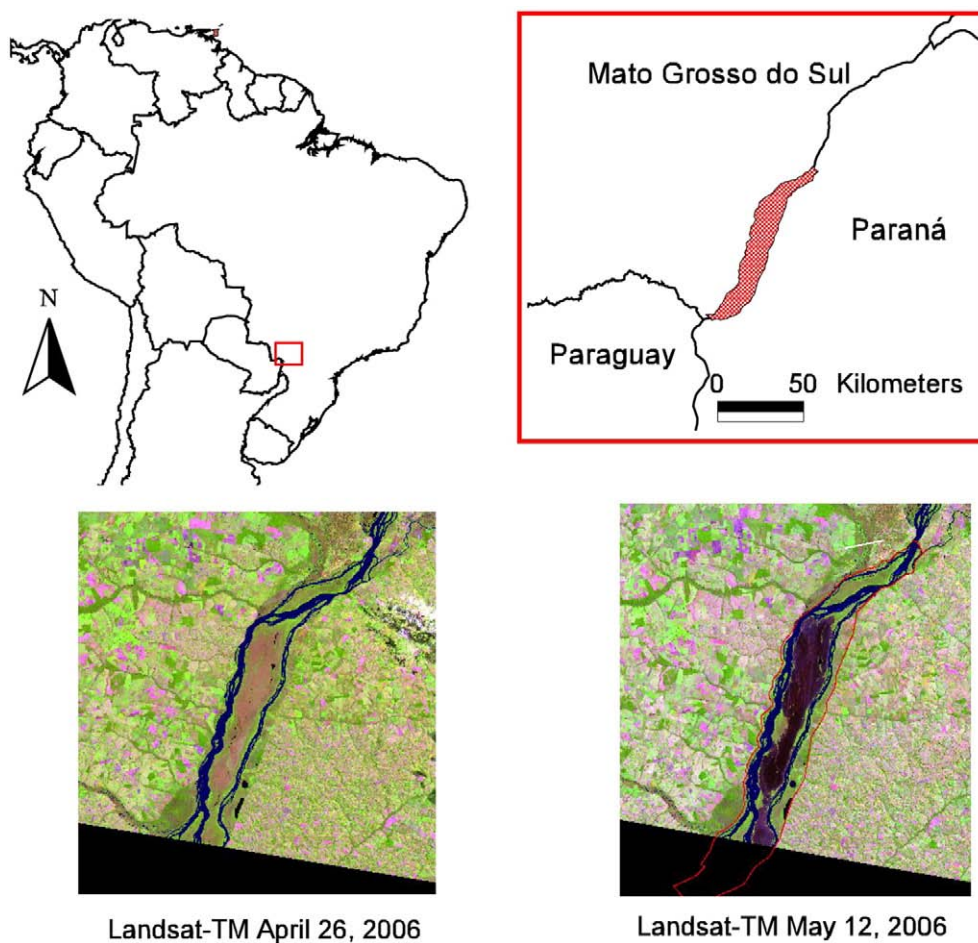


**Fig. 10.** Location of the Ilha Grande National Park, between the states of Paraná and Mato Grosso do Sul (upper right panel) in southwestern Brazil (upper left panel) and LANDSAT TM image (RGB 543) of the National park before the fire episode, on April 26, 2006 (lower left panel) and after the fire episode on May 12, 2006 (lower right panel). The outline of the National Park is shown in red.

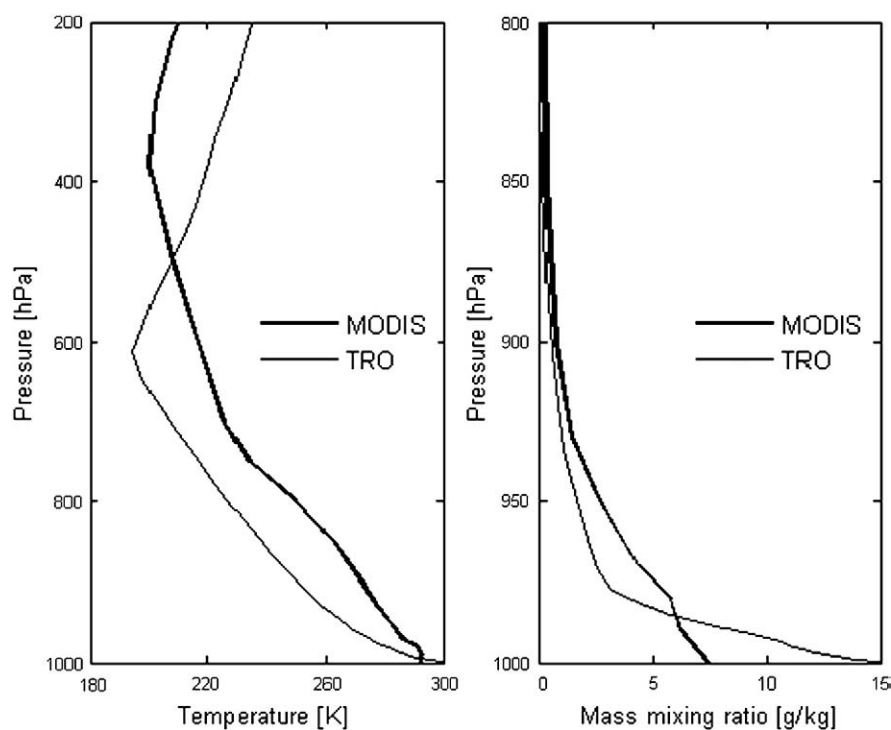


**Fig. 11.** MODIS mean profiles (bold curves) of temperature (left panel) and humidity (right panel) over Ilha Grande National Park on May 12, 2006. The TRO profile stored at MODTRAN-4 is also represented (thin curves).

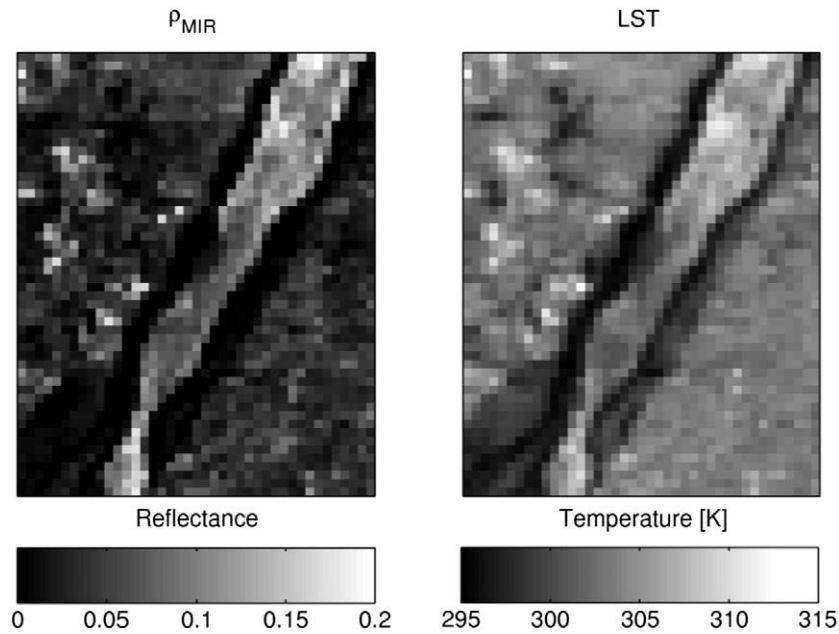


Fig. 12. Retrieved values of surface MIR reflectance (left panel) and LST (right panel) over the Ilha Grande National Park on May 12, 2006.

reflectance from TOA MIR radiance and TIR brightness temperature of the original images (May-12 environment) and of the synthetic ones (TRO and TRO-HOT environments).

The impact of using retrieved values to discriminate between burned and unburned surfaces for the three considered environments was evaluated by comparing the values of reflectance as retrieved by Eq. (10) over two sets of pixels representative of the two classes to be discriminated and then checking whether the respective statistical distributions allow distinguishing between the surfaces.

A set of 133 burned pixels, hereafter referred to as the burned class, was therefore selected from the scene, together with a set of 262 pixels that included the remaining land cover types (namely green vegetation, crop fields and water bodies), hereafter referred to as the

unburned class. Choice of pixels was made by visual comparison between two LANDSAT TM scenes (path/row 224/76) acquired on April 24 and May 12, 2006. Hot spots detected by INPE were also used in the process of selecting pixels associated to burned surfaces.

According to Kaufman and Remer (1994), a quantitative assessment of the effectiveness of the KR94 algorithm to discriminate between burned and unburned surfaces may be obtained with the following index:

$$M = \frac{|\mu_u - \mu_b|}{\sigma_u + \sigma_b} \quad (12)$$

where  $\mu_u(\mu_b)$  is the mean value and  $\sigma_u(\sigma_b)$  is the standard deviation for the unburned (burned) class. It is worth noting that index  $M$  may

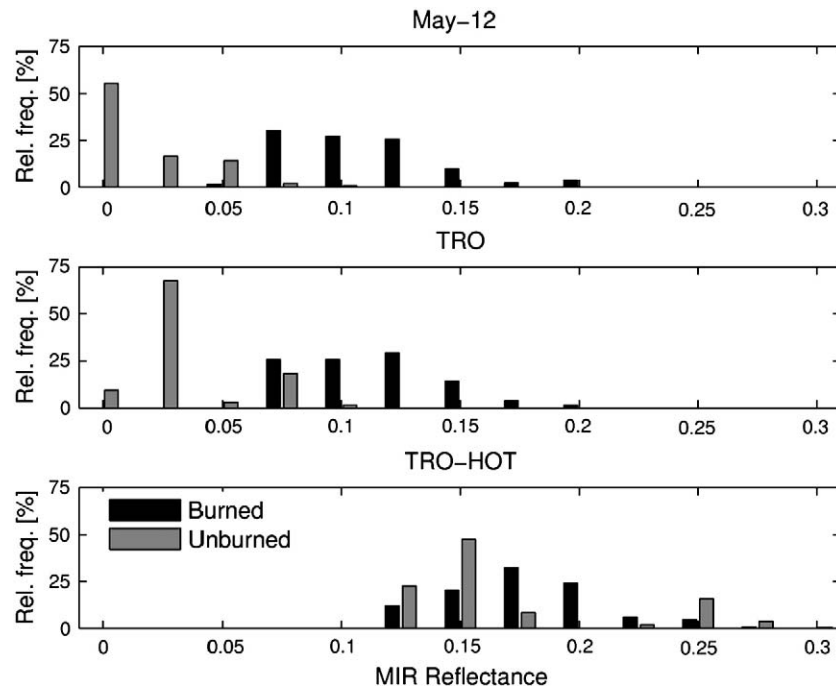


Fig. 13. Histograms of MIR reflectance for burned (black) and unburned (gray) classes as retrieved by means of Eq. (10) for May-12 (upper panel), TRO (middle panel) and TRO-HOT (lower panel) environments.

**Table 3**

Mean values,  $\mu_u(\mu_b)$ , and standard deviation,  $\sigma_u(\sigma_b)$ , of unburned (burned) surfaces and discrimination indices,  $M$ , for retrieved values of surface reflectance in the case of May-12, TRO and TRO–HOT environments.

	$\mu_u$	$\sigma_u$	$\mu_b$	$\sigma_b$	$M$
May-12	0.02	0.021	0.11	0.032	1.76
TRO	0.03	0.024	0.12	0.027	1.58
TRO–HOT	0.17	0.046	0.18	0.033	0.53

be viewed as an estimator of signal-to-noise ratio, the absolute difference between the mean values of the two classes representing the signal (associated to between-group variability) and the sum of the standard deviations representing noise (associated to within-group variability). Values of  $M$  larger than one indicate good separability, whereas values smaller than one represent a large degree of overlap between the values associated to the two classes.

Results are shown in Fig. 13 and Table 3. In the case of unburned surfaces, and when going from May-12 to TRO–HOT environments, there is a progressive shift of the histograms towards larger values of reflectance, accompanied by an increase of dispersion. Both shift and increase are especially pronounced from TRO to TRO–HOT. In strong contrast, in the case of burned surfaces, histograms of reflectance remain virtually unchanged when comparing May-12 to TRO environments, and there is a moderate shift when going from TRO to TRO–HOT environments. Moreover, the dispersion is virtually unaffected by injection of water vapor in the atmosphere and by surface temperature increase. The different sensitivity of the two types of surface leads to a progressive overlap of the histograms, which is translated by the decrease of  $M$ , from May-12 to TRO–HOT, and especially from TRO to TRO–HOT. In the latter type of environment  $M$  reaches a value of 0.53, an indication of very poor discriminant ability.

Results obtained for the fire event at the Ilha Grande National Park confirm those previously obtained with MODTRAN-4 simulations, namely that discrimination between burned and unburned surface based on values of surface reflectance retrieved with the KR94 algorithm is virtually impaired in the case of tropical regions for high values of surface temperature, especially when associated to low sun elevation angles. Since such circumstances are often present when using data from instruments on-board polar-orbiters (namely MODIS in Aqua and Terra) to identify burned areas over the Amazon and the adjacent “cerrado”, special care is required when using the KR94 algorithm.

## 5. Concluding remarks

Identification of burned areas over the Amazon and “cerrado” regions is a challenging task because of the ephemeral character of the radiative signal and the presence of aerosols that prevent using classical approaches e.g. based on red and near-infrared information. Middle-infrared (MIR) presents the advantage of being virtually unaffected by the presence of most types of aerosols, in particular those associated to biomass burning. In this respect the reflected component of MIR has proven to be especially adequate to discriminate between burned and unburned surfaces in mid-latitude regions (e.g. Pereira, 1999).

Kaufman and Remer (1994) proposed a methodology that presents the advantage of enabling for the retrieval of MIR reflectance with no need for auxiliary datasets or major computational means. The so-called KR94 algorithm, given by Eq. (10), has been specifically designed to retrieve MIR reflectance over dense dark forests in the middle latitudes. It has been also successfully applied to other types of surfaces and atmospheric environments, in particular for burned area discrimination (e.g. Barbosa et al., 1999; Roy et al., 1999). However, the quality of the retrieved values of MIR reflectance by Eq. (10) may significantly degrade when the relative contribution of the thermal emitted component to the total signal exceeds a threshold of about

75%. In the case of surfaces, such as vegetation, characterized by low values of MIR reflectance, the relative contribution of the solar component to the total MIR signal tends to be small, especially when the surface is hot (i.e. in case of relatively high values of LST). This contribution may be further reduced when the solar signal is weak due to low sun elevation angles (i.e. in case of high values of SZA). The above-mentioned aspects are especially relevant in tropical environments, where high land surface temperatures naturally dominate the scenes and pixels illuminated by low sun elevation angles are often present when using data from sensors on-board polar orbiters, in particular MODIS on-board Aqua and Terra.

Use of Eq. (10) in tropical environments to retrieve vegetation reflectance may lead to errors that are at least of the same order of magnitude of the reflectance to be retrieved and considerably higher for large values of LST and SZA. Under such conditions, retrieved values of reflectance for vegetation may attain those characteristic of charcoal making the two types of surface undistinguishable. Use of the KR94 algorithm becomes severely impaired and the complete radiative transfer equation, i.e. Eq. (3), should be used instead, provided the required auxiliary information is available about the surface (LST) and the atmospheric column (temperature and humidity profiles).

## Acknowledgments

This work was supported by the Portuguese Foundation of Science and Technology (FCT) (Grant No. SFRH/BD/21650/2005). R. Libonati's work was partially developed at the Satellite Division from the Brazilian National Institute for Space Research (DSA/INPE). We are grateful to Dr. Alberto Setzer (DSA/INPE) for valuable discussions and suggestions, to Dr. Fabiano Morelli and Jurandir Ventura (DSA/INPE) for making available LANDSAT and MODIS data, to José Carlos dos Santos (LCP/INPE) for collecting the samples of charcoal, and to Dr. Simon Hook (JPL/NASA) for performing the charcoal emissivity measurements. The authors also thank Dr. Brent Holben and his staff for their effort in establishing and maintaining Abracos Hill AERONET site. The vegetation spectral emissivity data were made available courtesy of the MODIS UCSB and ASTER Emissivity Libraries.

## References

- Baldrige, A. M., Hook, S. J., Grove, C. I., & Rivera, G. (2009). The ASTER Spectral Library Version 2.0. *Remote Sensing of Environment*, 113, 711–715.
- Barbosa, P. M., Gregoire, J. -M., & Pereira, J. M. C. (1999). An algorithm for extracting burned areas from time series of AVHRR GAC data applied at a continental scale. *Remote Sensing of Environment*, 69, 253–263.
- Berk, A., Anderson, G. P., Acharya, P. K., Chetwynd, J. H., Bernstein, L. S., Shettle, E. P., Matthew, M. W., & Alder-Golden, S. M. (2000). MODTRAN4 Version 2 User's Manual. Air Force Research Laboratory, Space Vehicles Directorate, Air Force Material Command, Hanscom AFB, MA (pp. 01731–03010).
- Boyd, D. S. (1999). The relationship between the biomass of Cameroonian tropical forests and radiation reflected in middle infrared wavelengths (3.0–5.0  $\mu\text{m}$ ). *International Journal of Remote Sensing*, 20, 1017–1023.
- Boyd, D. S., & Duane, W. J. (2001). Exploring spatial and temporal variation in middle infrared reflectance (at 3.75  $\mu\text{m}$ ) measured from the tropical forests of West Africa. *International Journal of Remote Sensing*, 22, 1861–1878.
- Boyd, D. S., Wicks, T. E., & Curran, P. J. (2000). Use of middle infrared radiation to estimate the leaf area index of a boreal forest. *Tree Physiology*, 20, 755–760.
- Chase, T. N., Pielke, R. A., Kittel, T. G. F., Nemani, R. R., & Running, S. W. (2000). Simulated impacts of historical land cover changes on global climate in northern winter. *Climate Dynamics*, 16, 93–105.
- Cihlar, J., Latifovic, R., Chena, J., Trishchenko, A., Duc, Y., Fedosejevs, G., & Guindona, B. (2004). Systematic corrections of AVHRR image composites for temporal studies. *Remote Sensing of Environment*, 89, 217–233.
- Crutzen, P. J., & Andreae, M. O. (1990). Biomass burning in the tropics: Impact on atmospheric chemistry and biogeochemical cycles. *Science*, 250, 1669–1678.
- Evangelista, H., Maldonado, J., Godoi, R. H. M., Pereira, E. B., Koch, D., Tanizaki-Fonseca, K., Van Grieken, R., Sampaio, M., Setzer, A., Alencar, A., & Gonçalves, S. C. (2007). Sources and transport of urban and biomass burning aerosol black carbon at the South-west Atlantic coast. *Journal of Atmospheric Chemistry*, 56, 225–238.
- Florinsky, I. V., Kulagina, T. B., & Meshalkina, J. L. (1994). Influence of topography on landscape radiation temperature distribution. *International Journal of Remote Sensing*, 15, 3147–3153.
- França, H., & Setzer, A. W. (1998). AVHRR temporal analysis of a savanna site in Brazil. *International Journal of Remote Sensing*, 19, 3127–3140.



- França, H., & Setzer, A. W. (2001). AVHRR analysis of savanna site through a fire season in Brazil. *International Journal of Remote Sensing*, 22, 2449–2461.
- Fraser, R. S., & Kaufman, Y. J. (1985). The relative importance of aerosol scattering and absorption in remote sensing. *IEEE Transactions on Geoscience and Remote Sensing*, 23, 525–533.
- Gesell, G. (1989). An algorithm for snow and ice detection using AVHRR data: An extension to the APOLLO software package. *International Journal of Remote Sensing*, 10, 897–905.
- Goita, K., & Royer, A. (1997). Surface temperature and emissivity separability over land surface from combined TIR and SWIR AVHRR data. *IEEE Transactions on Geoscience and Remote Sensing*, 35, 718–733.
- Holben, B. N., & Shimabukuro, Y. E. (1993). Linear mixing model applied to coarse spatial resolution data from multi-spectral satellite sensors. *International Journal of Remote Sensing*, 14, 2231–2240.
- Holben, B. N., Vermote, E., Kaufman, Y. J., Tanre, D., & Kalb, V. (1992). Aerosol retrieval over land from AVHRR data – Application for atmospheric correction. *IEEE Transactions on Geoscience and Remote Sensing*, 30, 212–222.
- Holben, B. N., Eck, T. F., Slutsker, I., Tanre, D., Buis, J. P., Setzer, A., Vermote, E., Reagan, J. A., Kaufman, Y. J., Nakajima, T., Lavenu, F., Jankowiak, I., & Smirnov, A. (1998). AERONET a federated instrument network and data archive for aerosol characterization – An overview. *Remote Sensing of Environment*, 66, 1–16.
- Jiang, G. -M., Li, Z. -L., & Nerry, F. (2006). Land surface emissivity retrieval from combined mid-infrared and thermal infrared data of MSG-SEVIRI. *Remote Sensing of Environment*, 105, 326–340.
- Jin, Y., & Roy, D. P. (2005). Fire-induced albedo change and its radiative forcing at the surface in northern Australia. *Geophysical Research Letters*, 32, L13401. doi:10.1029/2005GL022822.
- Kaufman, Y. J. (1995). Remote sensing of direct and indirect aerosol forcing. In R. J. Charlson, & J. Heintzenberg (Eds.), *Aerosol forcing of climate* (pp. 298–332). London: Wiley.
- Kaufman, Y. J., & Remer, L. (1994). Detection of forests using mid-IR reflectance: An application for aerosol studies. *IEEE Transactions on Geoscience and Remote Sensing*, 32(3), 672–683.
- Koren, I., Kaufman, Y. J., Remer, L. A., & Martins, J. V. (2004). Measurement of the effect of Amazon smoke on inhibition of cloud formation. *Science*, 303, 1342–1345.
- Lambin, E. F., & Geist, J. (2006). *Land-use and land-cover change – Local processes and global impacts, Series: Global Change – The IGBP Series*.
- Le Page, Y., Pereira, J. M. C., Trigo, R. M., DaCamara, C. C., Oom, D., & Mota, B. (2007). Global fire activity patterns (1996–2006) and climatic influence: An analysis using the World Fire Atlas. *Atmospheric Chemistry and Physics*, 8, 1911–1924.
- Li, Z. -L., & Becker, F. (1993). Feasibility of LST and emissivity determination from NOAA/AVHRR data. *Remote Sensing of Environment*, 43, 1–20.
- Luvall, J. C., & Holbo, H. R. (1991). Thermal remote sensing methods in landscape ecology. *Quantitative methods in landscape ecology, ecological studies* (pp. 127–152). New York: Springer-Verlag.
- Menon, S., Hansen, J., Nazarenko, L., & Luo, Y. (2002). Climate effects of black carbon in China and India. *Science*, 297, 2250–2253.
- MODIS Characterization Support Team – MCST (2006). *MODIS Level 1B Product User's Guide*: NASA/Goddard Space Flight Center available at <http://www.mcst.ssaai.biz/mcstweb/documents/M1054.pdf>.
- Nemani, R., Pierce, L., Running, S., & Goward, S. (1993). Developing satellite-derived estimates of surface moisture status. *Journal of Applied Meteorology*, 32, 548–557.
- Nerry, F., Petitcolin, F., & Stoll, M. -P. (1998). Bidirectional reflectivity in AVHRR channel 3: Application to a region in northern Africa. *Remote Sensing of Environment*, 66, 298–316.
- Nobre, C. A., Mattos, L. F., Derczynski, C. P., Tarasova, T. A., & Trosnikov, I. V. (1998). Overview of atmospheric conditions during the Smoke, Clouds, and Radiation-Brazil (SCAR-B) field experiment. *Journal of Geophysical Research*, 103, 31809–31820.
- Penner, J. E., Dickinson, R. E., & O'Neill, C. A. (1992). Effects of aerosol from biomass burning on the global radiation budget. *Science*, 256, 1432–1433.
- Pereira, J. M. C. (1999). A comparative evaluation of NOAA/AVHRR vegetation indexes for burned surface detection and mapping. *IEEE Transactions on Geoscience and Remote Sensing*, 37(1), 217–226.
- Pereira, J. M. C. (2003). Remote sensing of burned areas in tropical savannas. *International Journal of Wildland Fire*, 12, 259–270.
- Peres, L. F., & DaCamara, C. C. (2004). LST and emissivity estimation based on the two-temperature method: Sensitivity analysis using simulated MSG/SEVIRI data. *Remote Sensing of Environment*, 91, 377–389.
- Petitcolin, F., & Vermote, E. (2002). Land surface reflectance, emissivity and temperature from MODIS middle and thermal infrared data. *Remote Sensing of Environment*, 83, 112–134.
- Pielke, R. A., Sr., Marland, G., Betts, R. A., Chase, T. N., Eastman, J. L., Niles, J. O., Niyogi, D. D. S., & Running, S. W. (2002). The influence of land-use change and landscape dynamics on the climate system – Relevance to climate change policy beyond the radiative effect of greenhouse gases. *Philosophical Transactions of the Royal Society of London*, 360, 1705–1719.
- Prata, A. J., Caselles, V., Coll, C., Sobrino, J. A., & Ottle, C. (1995). Thermal remote sensing of LST from satellites: Current status and future prospects. *Remote Sensing Reviews*, 12, 175–224.
- Price, J. C. (1989). Quantitative aspects of remote sensing in the thermal infrared. *Theory and Applications of Optical Remote Sensing* (pp. 578–603). New York: John Wiley and Sons.
- Prins, E. M., Feltz, J. M., Menzel, W. P., & Ward, D. E. (1998). An overview of GOES-8 diurnal fire and smoke results for SCAR-B and 1995 fire season in South America. *Journal of Geophysical Research*, 103, 31821–31835.
- Reinhardt, T. E., Ottmar, R. D., & Castilla, C. (2001). Smoke impacts from agricultural burning in rural Brazilian Town. *Journal of the Air & Waste Management*, 51, 443–450.
- Roger, J. C., & Vermote, E. F. (1998). A method to retrieve the reflectivity signature at 3.75  $\mu\text{m}$  from AVHRR data. *Remote Sensing of Environment*, 64, 103–114.
- Rosenfeld, D. (1999). TRMM observed first direct evidence of smoke from forest fires inhibiting rainfall. *Geophysical Research Letters*, 26, 3105–3108.
- Roy, D. P., Giglio, L., Kendall, J. D., & Justice, C. O. (1999). Multi-temporal active-fire based burn scar detection algorithm. *International Journal of Remote Sensing*, 20, 1031–1038.
- Ruff, I., & Gruber, A. (1983). Multispectral identification of clouds and earth surfaces using AVHRR data. *Proceedings of the 5th Conference on Atmospheric Radiation, Baltimore, MD, October 31–November 4* (pp. 475–478). Boston, MA: American Meteorological Society.
- Salisbury, J. W., & D'Aria, D. M. (1994). Emissivity of terrestrial materials in the 3–5  $\mu\text{m}$  atmospheric window. *Remote Sensing of Environment*, 47, 345–361.
- Schutt, J. B., & Holben, B. N. (1991). Estimation of emittances and surface temperatures from AVHRR data. *Proceedings IGARSS 91, Helsinki, Finland* (pp. 1179–1181).
- Sellers, P. J., Bounoua, L., Collatz, G. J., Randall, D. A., Dazlich, D. A., Los, S. O., Berry, J. A., Fung, I., Tucker, C. J., Field, C. B., & Jensen, T. G. (1996). Comparison of radiative and physiological effects of doubled atmospheric CO<sub>2</sub> on climate. *Science*, 271, 1402–1406.
- Seemann, S. W., Borbas, E., Li, J., Menzel, W. P., & Gumley, L. M. (2006). *MODIS Atmospheric Profile Retrieval Algorithm Theoretical Basis Document* Madison: University of Wisconsin-Madison available at [http://modis-atmos.gsfc.nasa.gov/\\_docs/ATBD07:MYD07\\_ATBD\\_C005.pdf](http://modis-atmos.gsfc.nasa.gov/_docs/ATBD07:MYD07_ATBD_C005.pdf).
- Shimabukuro, Y. E., Holben, B. N., & Tucker, C. J. (1994). Fraction images derived from NOAA AVHRR data for studying the deforestation in the Brazilian Amazon. *International Journal of Remote Sensing*, 15, 517–520.
- Wang, Z. (1999). *MODIS Land-Surface Temperature Algorithm Theoretical Basis Document (LST ATBD): Version 3.3* Santa Barbara: University of California available at <http://www.icess.ucsb.edu/modis/atbd-mod-11.pdf>.
- Zhao, M., Pitman, A., & Chase, T. N. (2001). The impacts of land cover change on the atmospheric circulation. *Climate Dynamics*, 17, 467–477.